ADVANCED ENERGY MATERIALS

www.advenergymat.de

In-Liquid Plasma Modified Nickel Foam: NiOOH/NiFeOOH Active Site Multiplication for Electrocatalytic Alcohol, Aldehyde, and Water Oxidation

Jan Niklas Hausmann, Pramod V. Menezes, Gonela Vijaykumar, Konstantin Laun, Thomas Diemant, Ingo Zebger, Timo Jacob, Matthias Driess,* and Prashanth W. Menezes**

The oxygen evolution reaction (OER) and the value-added oxidation of renewable organic substrates are critical to supply electrons and protons for the synthesis of sustainable fuels. To meet industrial requirements, new methods for a simple, fast, environmental-friendly and cheap synthesis of robust, self-supported and high surface area electrodes are required. Herein, a novel in-liquid plasma (plasma electrolysis) approach for the growth of hierarchical nanostructures on nickel foam is reported on. Under morphology retention, iron can be doped into this high surface area electrode. For the oxidation of 5-(hydroxymethyl)furfural and benzyl alcohol, the iron-free, plasma-treated electrode is more suitable reaching current densities up to 800 mA cm^{-2} with Faradaic efficiencies above 95%. For the OER, the iron-doped nickel foam electrode reaches the industrially relevant current density of 500 mA cm^{-2} at 1.473 ± 0.013 V_{RHE} (60 °C) and shows no activity decrease over 140 h. The different effects of iron doping are rationalized using methanol probing and in situ Raman spectroscopy. Furthermore, the intrinsic activity is separated from the number of active sites, and, for the organic oxidation reactions, diffusion limitations are revealed. The authors anticipate that the plasma modified nickel foam will be suitable for various (electro)catalytic processes.

1. Introduction

The oxygen evolution reaction (OER) is critical for a sustainable energy economy, as it supplies protons and electrons for the most prominent fuel formation processes, the hydrogen evolution reaction (HER) and CO_2 reduction.[1–5] Partly, the OER can be replaced by economically more viable processes, where the electrons are supplied by value-added oxidations of organic molecules (hybrid water electrolysis).[3,4,6] For all processes, to be economically viable, the applied electrodes must operate at large current densities and elevated temperatures without degradation over long operating times.[7,8] For applications where free standing electrodes are used (traditional alkaline water electrolysis, organic electrosynthesis, the chloralkali process...), powder catalysts fixed with binders can be disadvantageous, as they usually neither meet the required mechanical and chemical stability nor are cost-effective in their manufacturing.[8] A more suitable alternative is the direct modification of metallic electrode substrate surfaces.[9–11] In this context, the most promising electrode substrate is conducting and cheap nickel foam (NF) which provides a porosity in the micrometer range (10–1000 µm).[12] The surface area and active sites of NF could be drastically enhanced by the formation of hierarchical nanostructures on its surface. Such a NF could potentially be applied for various electrocatalytic reactions without the need of any further catalyst to fulfil the industrial

J. N. Hausmann, G. Vijaykumar, M. Driess, P. W. Menezes
Department of Chemistry, Metalorganics and Inorganic Materials
Technische Universität Berlin
Straße des 17 Juni 135, Sekr. C2, 10623 Berlin, Germany
E-mail: matthias.driess@tu-berlin.de;
prashanth.menezes@mailbox.tu-berlin.de

P. V. Menezes, T. Jacob
Institute of Electrochemistry
Ulm University
Albert-Einstein-Allee 47, 89081 Ulm, Germany
E-mail: timo.jacob@uni-ulm.de

The ORCID identification number(s) for the author(s) of this article can be found under https://doi.org/10.1002/aenm.202202098.

DOI: 10.1002/aenm.202202098

K. Laun, I. Zebger
Department of Chemistry
Physical Chemistry/Biophysical Chemistry
Technische Universität Berlin
Straße des 17. Juni 135, Sekr. PC14, 10623 Berlin, Germany

T. Diemant, T. Jacob
Helmholtz-Institute Ulm (HIU) Electrochemical Energy Storage
Helmholtzstraße 11, 89081 Ulm, Germany

T. Jacob
Karlsruhe Institute of Technology (KIT)
P.O. Box 3640, 76021 Karlsruhe, Germany

P. W. Menezes
Material Chemistry Group for Thin Film Catalysis–CatLab
Helmholtz-Zentrum Berlin für Materialien und Energie
Albert-Einstein-Str. 15, 12489 Berlin, Germany

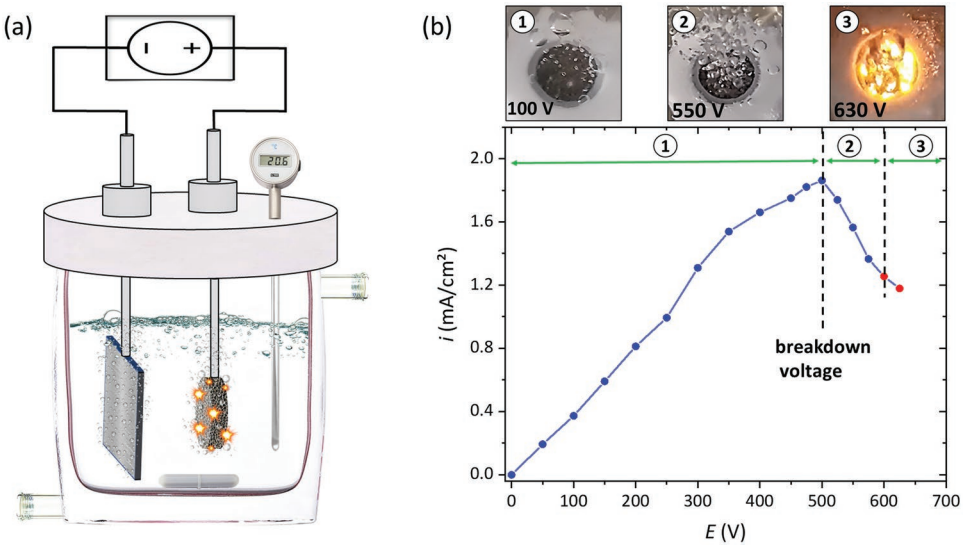

Figure 1. The plasma electrolysis process. a) The experimental setup of the in-liquid plasma treatment, a two-electrode setup with a high voltage power supply filled with 0.01 M KOH. b) The high potential electrical characteristics of NF in setup containing three regions: i) the conventional OER; ii) the transition; and iii) the plasma region. The images at the top show the NF in the three different potential regions with the characteristic glowing of the plasma in the region (iii).

requirements. However, the inert nature and high melting point of NF makes it challenging to modify and usually high externally applied temperatures and pressures are required (hydrothermal methods) or long reaction times of hours or days (immersion-based methods).[9,13,14]

To meet this challenge, we applied a novel, in-liquid (gas-liquid dual phase), thermal, glow discharge, and anodic plasma electrolysis (PE) approach that consumes little energy and takes only minutes. For this PE approach, a simple two-electrode setup is sufficient to achieve the surface modification within minutes. Furthermore, it does not require environmentally harmful chemicals or energy intensive external heating.[15] Recently, gas-phase plasma-based methods have been reported for the synthesis or modification of electrocatalysts.[16–18] In contrast to our approach, these methods are almost exclusively based on nonequilibrium ionized gases with low gas bulk temperatures (room temperature or below).[17,18] None of these plasma methods were applied directly to the electrode substrate, most likely because such non-thermal gas plasmas are not suitable for the surface nanostructuring of metals. During the herein used PE, local, instantaneous temperatures of up to 10 000 K were estimated and the pressure inside discharge channels could reach $\approx 10^2$–10^3 MPa while potentials of several hundred volts are applied.[19] We hypothesized that such conditions are ideal to form a chemically stable and nanostructured anode for electrocatalytic oxidation reactions, since a phase formed in such an environment, should easily endure the electrocatalytic conditions ($V < 2.0$) and thus overcome the persistent stability problem of OER catalysts.[20,21]

The herein reported PE approach creates a hierarchical, flower-like nanostructure on commercial NF. The modified NF is applied for the value-added selective oxidation of two organic substrates (5-(hydroxymethyl)furfural (HMF) and benzyl alcohol) reaching record high current densities of up to 800 mA cm^{-2}. Additionally, the PE modified NF shows a strongly increased OER activity compared to NF due to more accessible nickel sites. Without changing the morphology or surface area of the modified NF, we succeed in including iron showing that the plasma-treated NF can be chemically altered to be suitable for different catalytic reactions while profiting from its increased surface area. The iron modification leads to an increase of the intrinsic OER activity without significantly changing the accessible redox active sites. Combining PE treatment and iron-doping results in an OER activity enhancement of three orders of magnitude compared to NF at the same potential, and OER investigations at industrially relevant temperatures and current densities reveal a high long-term stability. However, for the organic oxidation reaction, the iron-free sample is more active. Consistent with previous reports and herein supported by in situ Raman spectroscopy and methanol (MeOH) probing, we propose an explanation for this phenomenon connecting the reaction intermediates of both processes with each other. Furthermore, we find that the OER activity is proportional to the number of redox active sites, while, in contrast, the organic substrate oxidation is diffusion-limited and its turnover scales with the double layer capacitance (C_{dl}) at high current densities.

2. Results

2.1. Plasma Treatment

Using the setup shown in **Figure 1**a, we investigated the anodic, high potential (0–630 V), electrical characteristics of NF in 0.01 M KOH (pH 11.96).[22] From the current–potential plot (Figure 1b), three regions can be classified: i) the conventional; ii) the transition; and iii) the plasma region. After the conventional OER region, the current drops due to the high resistance of the dense gas bubble formation at the electrodes. Eventually,

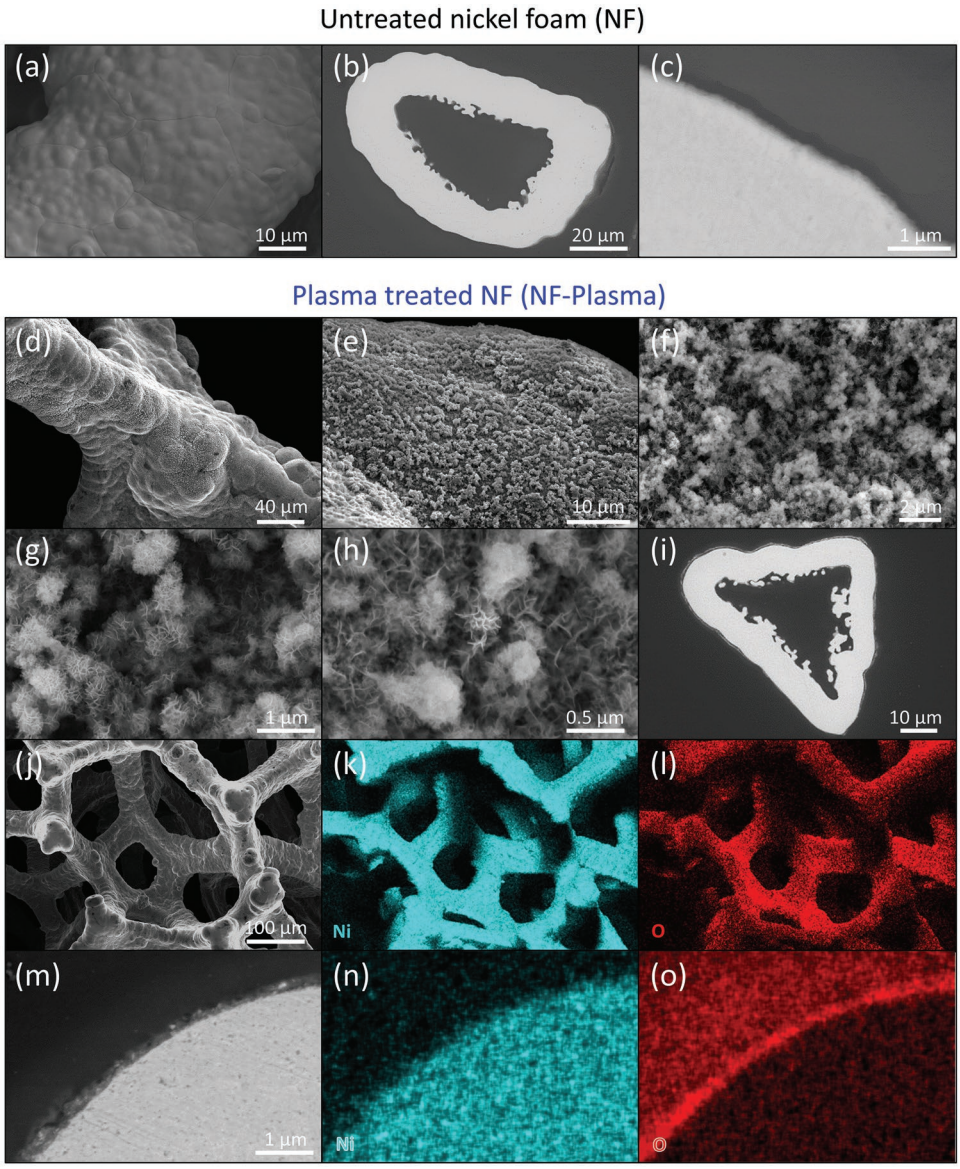

Figure 2. SEM investigations showing the plasma electrolysis induced morphology changes. SEM images with a top view (a) and cross section view (b,c) of untreated, commercially available nickel foam (NF). No hierarchical nanostructure or surface modification can be seen (see Figures S3–S6, Supporting Information, for more SEM images and elemental mappings). d–h) SEM images of NF after the plasma treatment from a top view showing the presence of hierarchical nanostructures (see Figure S7, Supporting Information, for more images). i) SEM image of the cross section of plasma-treated NF showing a thin, porous surface layer (see Figure S8, Supporting Information, for more images). j–l) SEM/EDX elemental mapping of the plasma-treated NF with a top view (see Figure S9, Supporting Information, for EDX spectrum), showing a homogeneous distribution of nickel and oxygen. m–o) SEM/EDX elemental mapping of the cross section of plasma-treated NF (see Figure S10, Supporting Information, for EDX spectrum) revealing an oxide surface layer. The cross-section images were taken of samples that were embedded into epoxy resin and grounded down to obtain cross-sections.

at a potential of 575 V, a uniform plasma-discharge is observed in the O_2 gas bubble region of the anode (see Figure 1b). Scanning electron microscopy (SEM) images reveal that a voltage of 630 V applied for 10 min is most suitable for the formation of a homogeneously nanostructured surface (Figures S1 and S2, Supporting Information). For the applied parameters (630 V, 0.6 A, 10 min) and assuming an electricity price of 0.15 US$ per kilowatt-hour, a low energy consumption of 63 Wh and a small electricity cost below 0.02 US$ per centimeter square electrode is obtained.

2.2. Morphology, Redox Activity, and Surface Area

SEM shows that untreated NF has a flat surface, and, in the cross section, no surface oxide layer can be seen (**Figure 2**a–c and Figures S3–S6, Supporting Information). After plasma treatment (NF-Plasma), a hierarchical nanostructure is visible consisting of 0.1–1 µm large spherical objects that stack on each other, partly agglomerate, and form a thick, homogeneous layer covering the entire NF surface (Figure 2d–i and Figures S7–S10, Supporting Information). Larger magnifications reveal that

these spheres consist of smaller nano petals that are only a few nanometers thick and give the spheres a flower-like appearance. Cross section images reveal an ≈200–500 nm thick, porous surface layer (Figure 2i,m, and Figure S8, Supporting Information). SEM energy dispersive X-ray (EDX) mappings demonstrate a homogenous distribution of Ni and O and the respective EDX spectrum contains a clear oxygen peak compared to the one of untreated NF (Figure 2j–l, and Figures S4 and S9, Supporting Information). An EDX mapping of the cross section shows that the porous surface layer contains Ni and O (Figure 2m–o, and Figure S10, see Figure S6, Supporting Information, for untreated NF). For NF and NF-Plasma, cyclic voltammetry (CV) in 1 M KOH revealed reversible redox features that can be assigned to the oxidation of Ni^{II} (Figure S11a, Supporting Information).[23–26] Integration of the reduction peak yields an increase of the nickel redox activity by around 40 times through the plasma treatment (Figure S11b,c, Supporting Information), and the double layer capacitance (C_{dl}) increased around six times (Figures S11e and S12, Supporting Information).

2.3. Iron Doping

Iron doping was achieved by cycling NF-Plasma in $Fe(NO_3)_3$ saturated 1 M KOH (Figure S12a, Supporting Information). Ten CV cycles were chosen as the OER activity merely changed after the tenth cycle. This treatment increases the redox peak potential while the current maximum height remained almost the same (Figures S11c and S12a, Supporting Information) which is typical for iron doping at easily accessible edge or defect sites of nickel oxyhydroxides.[27] It is reported that such an incorporation leads to dramatically improved OER activity but only marginally affects the majority of the nickel redox species that reside surrounded by six nickel atoms within a layer and most likely do not participate in catalysis.[27] SEM images taken after the iron incorporation into a NF-Plasma sample show that the morphology was unaltered (Figure S13, Supporting Information). Furthermore, SEM/EDX analysis reveals the presence of iron and potassium and shows a homogeneous distribution of Ni, Fe, K, and O (Figure S14, Supporting Information). Also, the C_{dl} remains almost unchanged by the iron doping (Figure S12b, Supporting Information).

2.4. PXRD and XPS

The powder X-ray diffractogram (pXRD) contains only reflexes of metallic nickel. Thus, the newly formed $Ni(Fe)O_xH_y$ phases are all amorphous (Figure S15, Supporting Information). For all three samples, the X-ray photoelectron spectra (XPS) in the Ni 2p region are consistent with the presence of a Ni^{II} surface species (**Figure 3**a).[28,29] Only for the NF-Plasma-Fe sample, a clear Fe 2p doublet with a binding energy typical for Fe^{III} is present (Figure 3b).[29] The O 1s spectrum of NF is consistent with mainly hydroxide species and adsorbed water (Figure 3c).[30,31] The O 1s spectra of NF-Plasma and NF-Plasma-Fe indicate also these two species but additionally have a shoulder at lower binding energy which can be assigned to metal oxide (O^{II-}). The elemental surface composition determined from the XPS measurements reveals that 26 at% of iron compared to nickel were incorporated through the CVs (Figure 3c). In principle, as a potential of 630 V was applied during the plasma treatment, nickel phases with higher oxidation states are expected but only Ni^{II} was observed by XPS. The nickel at the surface most likely reacted with air forming Ni^{II} after the plasma treatment. Below the surface Ni^{II}, XPS depth profiling detects nickel in higher oxidation states (mainly NiOOH) and ultimately the main species is Ni° from the metallic NF beneath the surface oxide layer (Figure 3e).

2.5. OER Activity and Stability

The electrocatalytic OER properties in 1 M KOH of four samples were measured and compared (NF, NF-Fe, NF-Plasma, and NF-Plasma-Fe; see **Figure 4**a for an overview). The reverse scan of the CV measurements reveals the activity trend NF < NF-Plasma = NF-Fe < NF-Plasma-Fe with NF-Plasma-Fe yielding the current densities 10, 100 and 500 mA cm^{-2} at 207 ± 4, 248 ± 5 and 304 ± 11 mV overpotential, respectively (Figure 4b and see Figure S16a, Supporting Information, for data without iR correction). This OER activity trend is confirmed by the diameter of the Nyquist plots obtained by electrochemical impedance spectroscopy (Figure S16b, Supporting Information). To provide a meaningful comparison, we investigated several previously published iron-nickel catalysts as well as iridium and ruthenium oxides under the same conditions (Figure 4c and Figure S17, Supporting Information).[11,32] The NF-Plasma-Fe electrode shows the lowest overpotential of all studied systems. Besides activity, a critical parameter is the long-term stability at industrially relevant current densities. Thus, we performed a chronopotentiometry (CP) stability test at 200 mA cm^{-2} for 140 h showing a stable overpotential of 275 ± 5 mV (Figure 4d). Further improvements can be achieved by operating at elevated temperatures like in industrial systems. The potential required to reach 500 mA cm^{-2} is reduced by 60 mV to 1.473 ± 0.013 V_{RHE} when the temperature is increased to 60 °C (Figure 4e). A stability test at 60 °C and 400 mA cm^{-2} also shows no decline in activity (Figure 4e, inset).

2.6. Tafel Analysis and OER Activity Normalization

Steady-state Tafel measurements reveal small Tafel slopes of 32 and 34 mV/dec for the iron-doped samples and Tafel slopes of 43 and 46 mV/dec for the samples without intentional iron incorporation (Figure 4f). For rigorous iron-free nickel oxyhydroxides, Tafel slopes of ≈70–110 mV/dec are typical.[33,34] The inclusion of iron then continuously decreases this slope to ≈30 mV/dec.[34] Commercially available NF foam is never completely iron-free and the NF used by us contains 0.008 wt% (80 ppm) iron while the 1 M KOH contained <0.05 ppm Fe. Thus, the Tafel slopes observed by us are in accordance with nickel oxyhydroxide with iron traces (NF and NF-Plasma) and with nickel–iron oxyhydroxides close to an optimum nickel–iron ratio for the OER (NF-Fe and NF-Plasma-Fe).[33,34] Most importantly, the similar Tafel slope values indicate that the plasma treatment does not alter the reaction mechanism or the

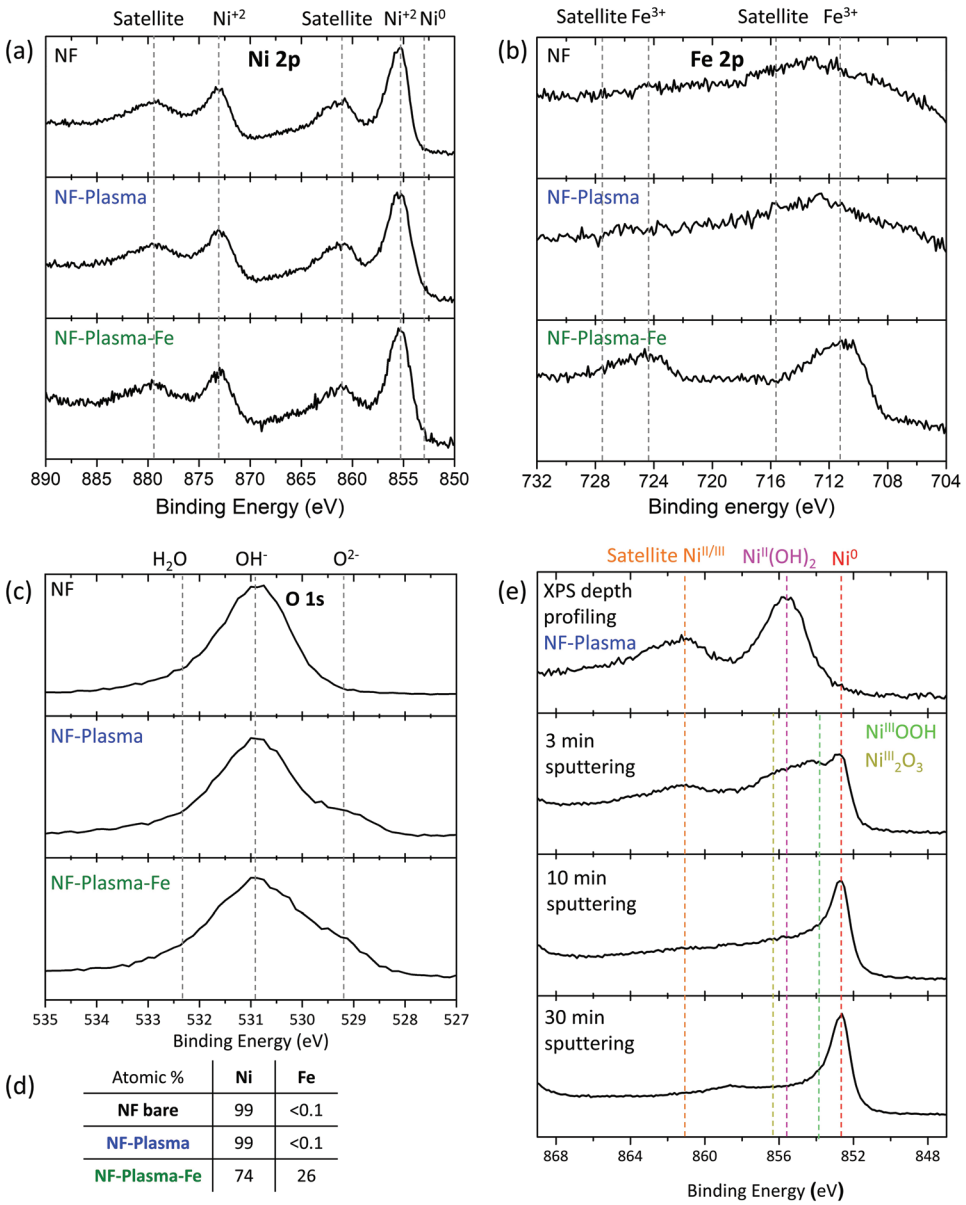

Atomic %	Ni	Fe
NF bare	99	<0.1
NF-Plasma	99	<0.1
NF-Plasma-Fe	74	26

Figure 3. The core-level XPS analysis of NF, NF-Plasma, and NF-Plasma-Fe. The Ni 2p spectra (a) of all films show two dominant $2p_{3/2}$ and $2p_{1/2}$ peaks with accompanying satellites typical for $Ni^{II}(OH)_2$.[28,29] The presence of Fe can only be found for NF-Plasma-Fe and the observed doublets in the Fe 2p spectrum (b) correspond to a Fe^{III} species.[29] The O 1s spectra (c) of NF-Plasma and NF-Plasma-Fe display similar peaks responsible for metal oxide, hydroxides, and adsorbed water while NF spectrum mostly shows surface hydroxide species.[30,31] The XPS quantification of Ni and Fe content of NF-Plasma-Fe on the surface is given in (d). e) The Ni 2p XPS depth profiling of NF-Plasma at three different sputtering times where the amount of hydroxide and oxide peaks diminished continuously with subsequent increase of Ni^0 species.[28,29]

nature of the active site. Nevertheless, one clear effect of the plasma treatment on the Tafel plot can be seen: the plasma-treated samples possess a linear behavior until current densities of 500 mA cm^{-2} while the non-treated samples show deviation from linearity starting at 10–30 mA cm^{-2}. The earlier deviation from linearity indicates that additional effects to the molecular kinetics inhibit the OER for these samples which could be mass transport limitations (hydroxide or oxygen diffusion, oxygen bubble detachment) or a too high surface intermediate coverage caused by the smaller surface area and number of active sites. As redox active sites fulfill various prerequisites for the OER (being anodically wired, having access to electrolyte [proton transfer], having an ability to change the oxidation state)[35] and considering that similar Tafel slopes indicate similar reaction mechanisms/active sites, we normalized the steady state OER data by the number of nickel redox active sites obtained by integration of the redox peak (Figure 4g).[21,26] With this normalization, the two iron-doped electrodes have a similar activity as well as the two non-incorporated ones. Furthermore, we calculated the O_2 turnover frequencies of the four catalysts based on the number of redox active nickel centers (Figure 4g, *y*-axis on the right).[26]

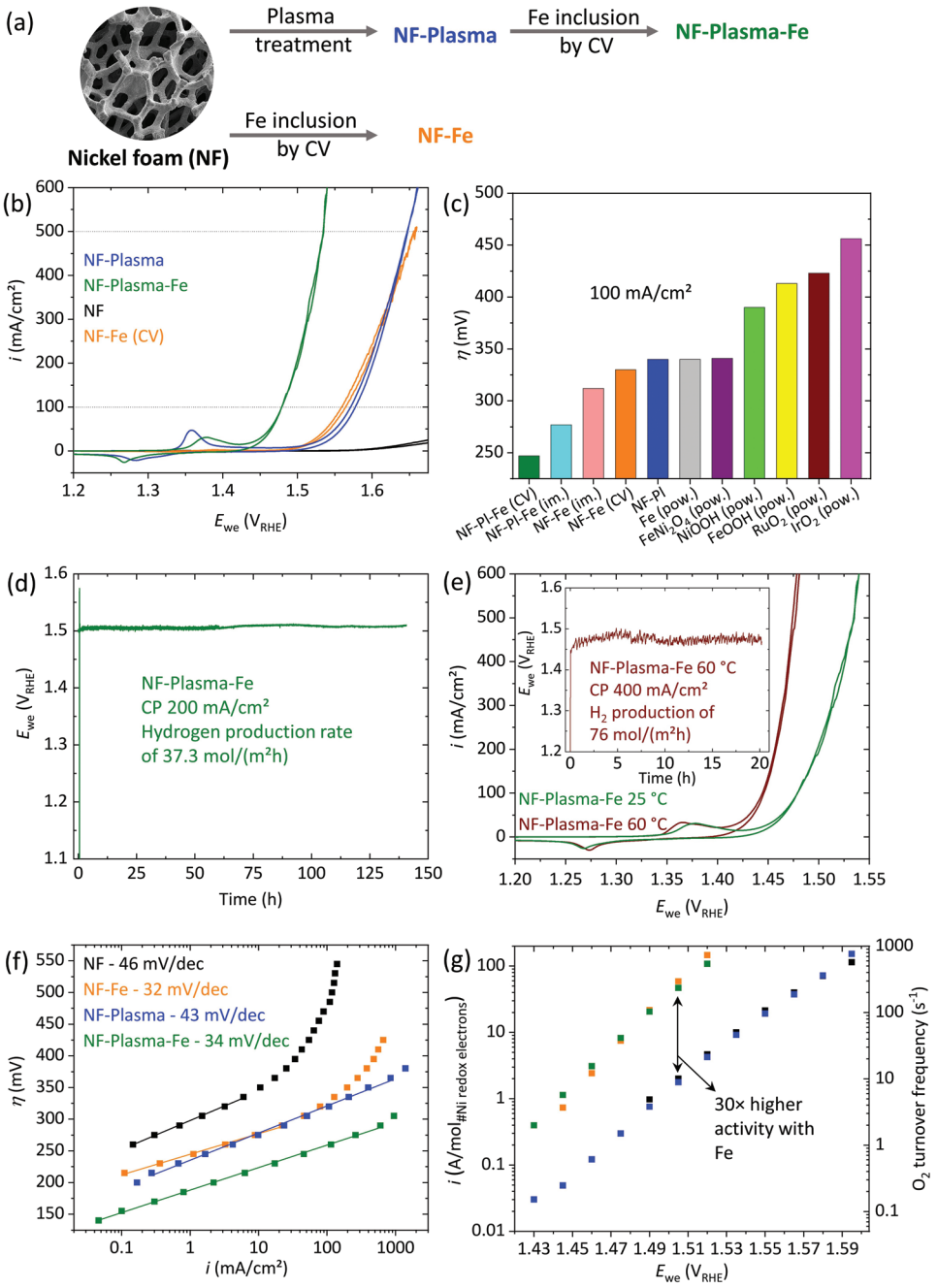

Figure 4. Electrochemical characterization. All measurements are with *iR* compensation (see Supporting Information for details). a) Overview of the samples that were electrocatalytically investigated. b) Cyclic voltammograms at a scan rate of 5 mV s^{-1}. c) Comparison of the overpotentials at 100 mA cm^{-2} with various other Ni-, Fe-, NiFe-, and noble metal-based catalysts (see Figure S17, Supporting Information, for details).[32] The loading of the powder samples was (0.8 mg cm^{-2}). Immersion means that the iron doping was performed by simple immersion in a 20 $mmol^{-1}$ aqueous $Fe(NO_3)_3$ solution for 4 h, as reported previously.[11] d) CP stability test at 25 °C with the hydrogen production rate (see Supporting Information for details). e) CV and CP stability test at 60 °C. f) Tafel slopes from steady-state CA measurements. g) Normalization of the data of Figure 4f by the number of redox active sites from the reduction peaks of Figures S11 and S12a, Supporting Information, and O_2 turnover frequency data based in the number of redox active nickel sites (more information on the calculations can be found in the Supporting Information and ref. [26]).

2.7. Post OER Analysis

XPS and SEM investigation of the NF-Plasma-Fe samples after 24 h at 200 mA cm^{-2} showed no change in the chemical nature or morphology of the sample, which is reasonable considering that the as prepared phases were formed under much harsher alkaline anodic conditions already (Figures S18 and S19, Supporting Information).

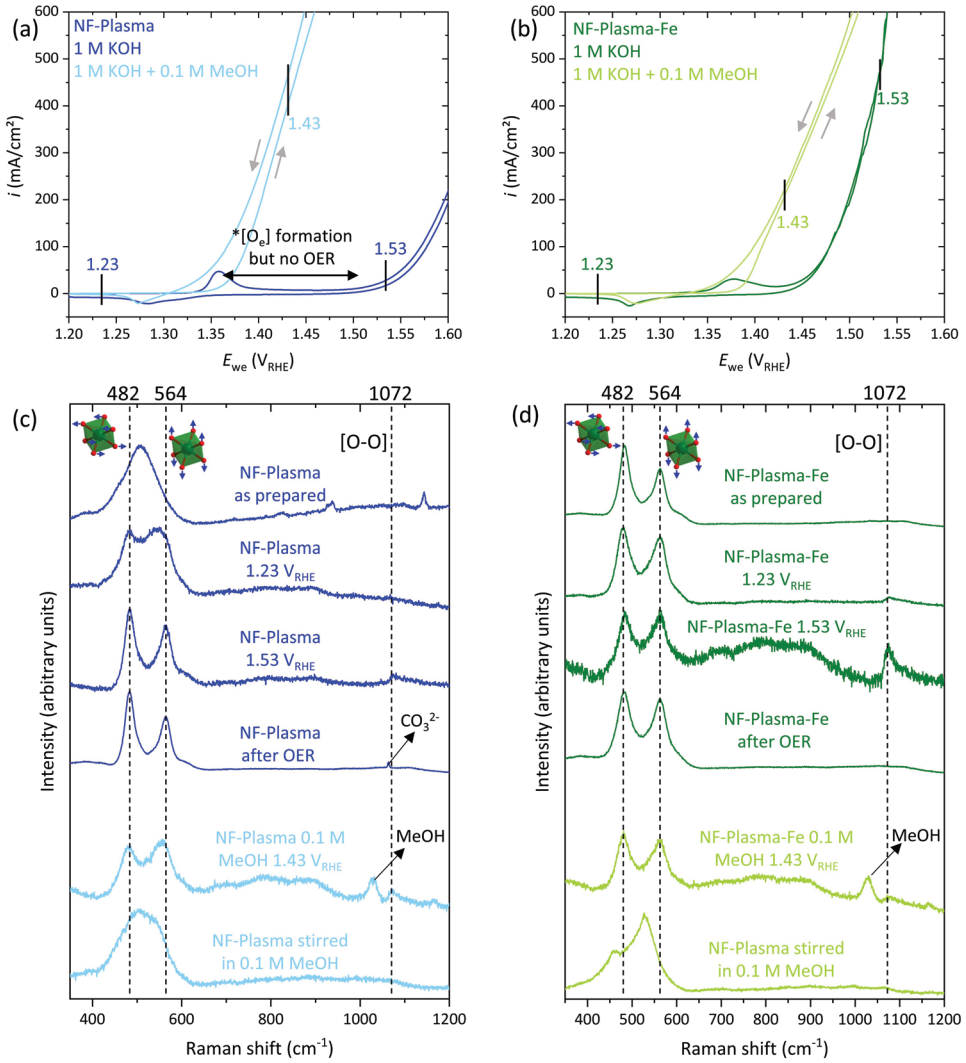

Figure 5. Methanol (MeOH) probing and in situ Raman spectroscopy. CVs (5 mV s^{-1}, stirring) in 1 M KOH with and without MeOH of NF-Plasma (a) and NF-Plasma-Fe (b). The grey arrows mark the scan direction. The addition of MeOH leads to much higher current densities assigned to the oxidation of MeOH through an electrophilic oxygen intermediate (*[O$_e$]). In situ Raman spectra taken at various potentials shown in (a) and (b) of NF-Plasma (c) and NF-Plasma-Fe (d). The vertical dashed lines mark the three most prominent vibrations and their assignment to vibrations of the [NiO$_6$] octahedra of Ni(Fe)OOH (Ni/Fe in green and O in red) and a previously reported [O-O] vibration.[38,39]

2.8. Methanol (MeOH) Probing and In Situ Raman Spectroscopy

Recently, Liu et al. suggested MeOH as a probing molecule for electrophilic oxygen species (*[O$_e$]) on a catalyst surface (see Supporting Information for a discussion on the nature of this species).[36] In this regard, for NF-Plasma and NF-Plasma-Fe, we recorded CVs with and without MeOH in 1 M KOH (**Figure 5**a,b). For both catalysts, in the presence of MeOH, high current densities are observed between the nickel redox feature and the OER onset of the MeOH free CVs probing *[O$_e$]. In this range, MeOH oxidation occurs and no bubbles form at the anode, as previously reported.[37] The addition of iron has three effects: i) it decreases the current density of selective MeOH oxidation (the current density at 1.43 V_{RHE} is around two times higher for NF-Plasma); ii) it shifts the redox peak anodically; and iii) it shifts the OER onset to higher potentials. Thus, NF-Plasma-Fe oxidizes MeOH slower and the potential range and maximum potential where MeOH oxidation without OER interference occurs is narrower making NF-Plasma the better alcohol oxidation catalyst. Furthermore, for NF-Plasma and NF-Plasma-Fe, the current density for the backward scan (from high to low potential) is higher than the one of the forward scan indicating that the electrode is transformed into a more active state for MOR-oxidation catalysis (most likely involving a higher oxidized catalyst).

In and ex situ Raman data was recorded at various potentials and different conditions of NF-Plasma (Figure 5c) and NF-Plasma-Fe (Figure 5d). Consistent with the XPS results, the Raman spectrum of as prepared NF-Plasma exhibits the typical Ni^{II}—O vibration of dehydrated or disordered nickel hydroxide along with small features that could be related to a nickel oxide.[38,40–42] When applying an increased anodic

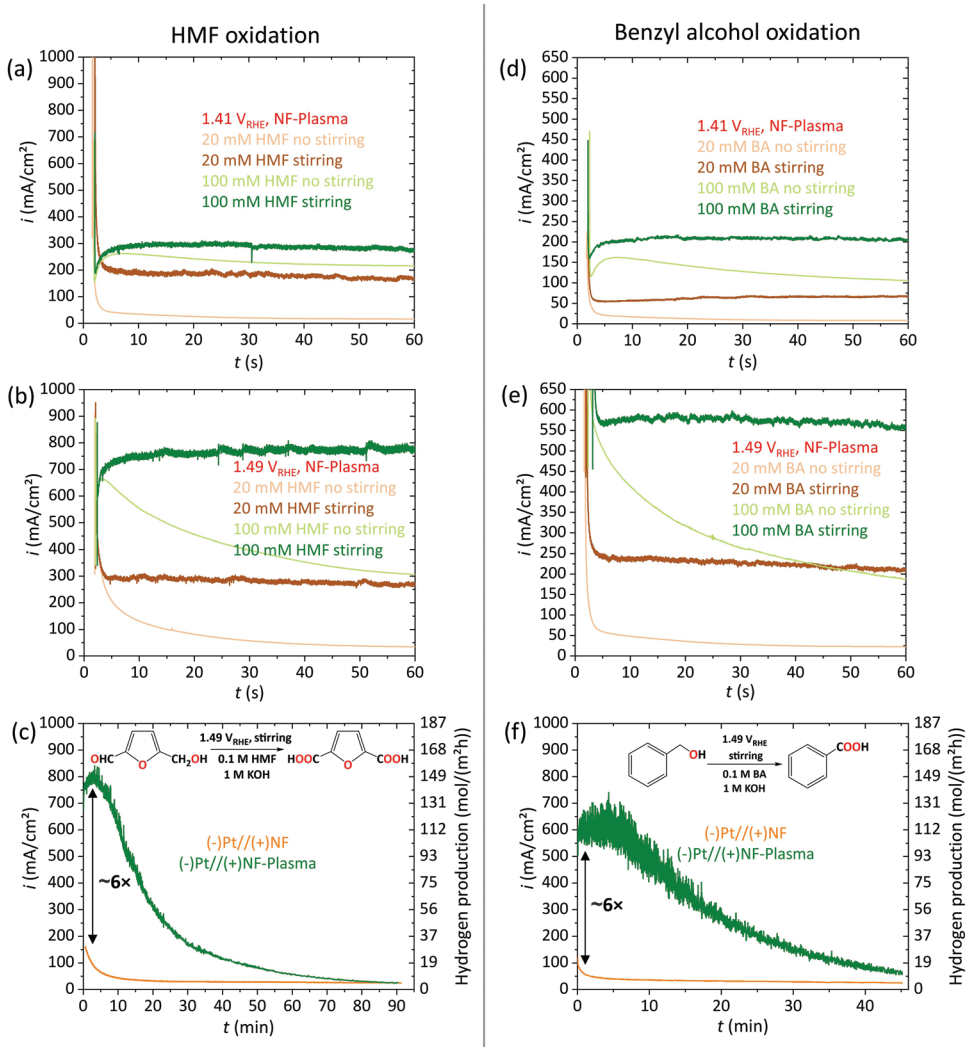

Figure 6. Organic oxidation reactions. CA measurements of 1 M KOH solutions with NF-Plasma with either 5-(hydroxymethyl)furfural (HMF) or benzyl alcohol (BA) at different concentrations, with and without stirring, and at different potentials. The inset in (c) shows the reaction occurring in (a–c). The inset in (f) shows the reaction occurring in (d–f). The CA measurements shown in (c) and (f) were terminated after exactly the charge was passed required for full product formation. After that ^{1}H-NMR spectroscopy was performed (Figures S22 and S23, Supporting Information). (c) and (f) include the hydrogen production rate (for details on the calculation see the Supporting Information).

potential, the Ni^{II}—O vibration vanishes, and two other bands related to the bending $\delta(Ni^{III}—O)$ (482 cm^{-1}) and stretching $\nu(Ni^{III}—O)$ (564 cm^{-1}) vibrations typical for NiOOH appear. Furthermore, at 1.53 V_{RHE}, a peak previously assigned to an [O-O] vibration is present at 1072 cm^{-1}.[38,39] For NF-Plasma-Fe, the same vibrational modes can be observed, in line with the presence of a Ni(Fe)OOH phase. Comparing the various Raman spectra, differences in the intensity ratios of the bands observed at 482 and 564 cm^{-1} are detectable. In this regard, decreasing I_{482}/I_{564} ratios have been correlated to higher iron contents.[34] Furthermore, such a decrease can also be caused by Ni—OH deprotonation and by higher nickel oxidation states which both can be induced by anodic potentials.[43] These trends are further confirmed herein: iron incorporated samples show lower I_{482}/I_{564} ratios, and, for NF-Plasma and NF-Plasma-Fe, the I_{482}/I_{564} ratio is smaller, for the in situ OER spectra at 1.53 V_{RHE} in comparison to the measurements accomplished ex situ after OER. The spectra recorded during MeOH oxidation exhibit the same features as those monitored during OER, including the [O-O] vibration, but reveal an additional band at 1026 cm^{-1} characteristic for MeOH. For NF-Plasma during MeOH oxidation, the $\nu(Ni^{III}—O)$ vibration is red-shifted and the I_{482}/I_{564} ratio is comparable to the one observed in the spectrum acquired without MeOH at a more cathodic potential (1.23 V_{RHE}) than the nickel redox feature indicating a lowered nickel oxidation state. Comparing the spectra after OER (1 h under air and at room temperature) to the ones after stirring in 0.1 M MeOH for 5 min, it is obvious that, after OER, the spectral features of NF-Plasma and NF-Plasma-Fe resemble those of Ni^{III}(Fe)OOH species, while after MeOH stirring, they are similar to the $Ni^{II}O_xH_y$ phase (see NF-Plasma as prepared).[38,40–42] As already reported, this shows that MeOH can reduce NiOOH to $Ni(OH)_2$ (potential independent mechanism).[44,45]

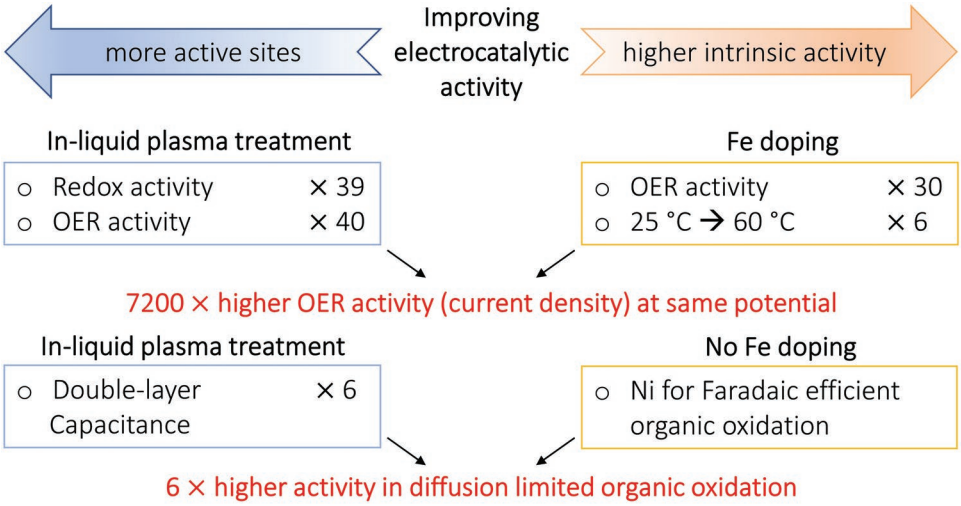

Figure 7. Two ways to improve the activity of an electrocatalyst. Herein, the number of active sites was increased using an in-liquid plasma treatment, and the intrinsic activity was tuned by iron doping and by increasing the temperature. Compared to bare NF at RT, the OER activity was 7200 times larger at the same potential versus RHE. For the OER, the iron-containing electrodes were 30 times more active than the one without; for the alcohol/aldehyde oxidation, it was the other way around and the iron-free electrodes showed an around two times higher activity at the same potential.

2.9. Value-Added Selective Oxidation of 5-(hydroxymethyl) furfural (HMF) and benzoic acid (BA)

Inspired by the high current densities and large potential range for the selective oxidation of MeOH, we investigated the value-added oxidation of benzyl alcohol (BA) and 5-(hydroxymethyl)furfural to benzoic acid and 2,5-furandicarboxylic acid (FDCA), respectively (see **Figure 6**c,f for reaction equations). Benzoic acid is a widely applied chemical with an annual production of more than 640 kt and so far relies on the resource- and energy-intensive toluene oxidation process.[46,47] HMF is a biomass-derived substrate and FDCA can be used as a precursor for polymers.[32,48] Thus, electrocatalytic HMF oxidation is a route to sustainable polymers.

First, in 1 M KOH without stirring, LSVs were recorded with NF-Plasma or NF (reference) as working electrode and with or without 0.1 M HMF (Figure S20, Supporting Information) or BA (Figure S21, Supporting Information). Like for MeOH, the LSVs reveal a potential range where HMF/BA oxidation occurs before the OER onset. Furthermore, for industrial applications, the transformation rate is crucial. We find that the HMF/BA oxidation rate depends on stirring, substrate concentration, and potential under steady-state high current density conditions (Figure 6). Based on these investigations, we performed bulk CA electrolysis experiments with the intention of full conversion of both substrates at a potential just below the OER onset (1.49 V_{RHE}). The achieved current densities are larger than previously reported ones reaching 800 and 600 mA cm^{-2} for 0.1 M HMF and BA, respectively.[32,49–51] Over time, the current decreases due to reduced substrate concentration. After exactly the required amount of charge for full conversion was passed (578.91 C for HMF and 385.94 C for BA), ^{1}H-NMR spectroscopy reveals >95% transformation for HMF (<5% non-electrochemical degradation product was detected as reported previously in 1 M KOH, Figure S22, Supporting Information)[50] and 96% isolated yield for BA could be obtained (Figure S23, Supporting Information). Thus, for both reactions, Faradaic efficiencies of above 95% were achieved. NF also shows some oxidation activity but with a six times lower current density, and a ^{1}H-NMR spectrum acquired after the same time as for NF-Plasma reveals various products together with only partial substrate consumption (Figure 6c,f, and Figures S22 and S23, Supporting Information).

3. Discussion

We have successfully increased the surface area, number of redox active sites, and C_{dl} of NF by creating a hierarchically nanostructured surface with a flower-like appearance. Such a high surface area NF can be suitable for various electrocatalytic reactions. Furthermore, after the plasma treatment, we have incorporated iron without changing the morphology indicating that the plasma-treated NF can potentially be chemically modified to be suitable for various catalytic processes. For the OER, the plasma treatment and iron doping lead to an activity enhancement of three orders of magnitude comparing current densities at the same potential. XPS, powder X-ray diffractogram (pXRD) and in situ Raman data show that similar NiOOH or $Ni_xFe_{1-x}OOH$ are formed during OER for all samples. To explain the high activities and their differences, the two most important parameters to improve the turnover frequency of a catalytic system (electrode) must be separated and quantified (**Figure 7**). The first one is to increase the number of active sites and the second one to enhance the intrinsic activity per active site. In this regard, we investigated four electrodes (Figure 4a). The two electrodes without (NF and NF-Plasma) and the two with iron doping (NF-Fe and NF-Plasma-Fe) have a similar Tafel slope indicating the same reaction mechanism and same kind of active sites/phase. As redox active sites fulfil various prerequisites for the OER (being anodically wired, having access to electrolyte [proton transfer], having an ability to change the oxidation state),[35] we normalized the steady-state OER data by the number of nickel redox

active sites obtained by integration of the redox peak (e^-_{redox}, Figure 4g).[21,26] This normalization results in similar currents for NF and NF-Plasma as well as NF-Fe and NF-Plasma-Fe. Thus, NF and NF-Plasma have the same kind of active sites/phase and the number of active sites is proportional to e^-_{redox}. The same is true for the pair NF-Fe and NF-Plasma-Fe. In general, the plasma treatment leads to a 40-time increased number of catalytic active sites. We note here that this proportional relation does not necessarily mean that all redox active nickel sites are catalytically active or have the same turnover frequency. Consistent with previous reports on NiO_xH_y phases,[52] iron doping leads to a changed Tafel slope and a 30-time increased activity per e^-_{redox} indicating a higher intrinsic catalytic activity per active site. Combining these two effects with an increase of the electrolyte temperature to 60 °C results in an increase of the OER activity by $30 \times 40 \times 6 = 7200$ times compared to untreated NF at the same potential at 25 °C and positions NF-Plasma-Fe among the most active, recently benchmarked OER catalysts (Figures 7 and 4c).[9]

For the oxidation of alcohols and aldehydes in 0.1 M KOH, two reaction mechanisms were proposed by Choi et al.[4,45,53] One is potential independent meaning that the current density does not increase with increasing anodic potential after the onset. In this mechanism, the NiOOH reacts as a chemical oxidation reagent in the rate-determining step (rds) and the role of the applied potential is merely to regenerate NiOOH. The other one is potential dependent, which is favored at higher pH values (herein 1 M KOH is used) and involves the oxidation of [Ni^{III}—O^{-II}]. In [Ni^{III}—O^{-II}] oxidation, the [O^{-II}] ligand cannot be considered redox innocent and various works have shown that oxygen species with electrophilic character is formed.[23,24,36,38,40,39,54] It has been suggested that the formation of electrophilic oxygen (*[O_e], see Supporting Information for a discussion on the nature of this species) from water or hydroxide is the initial reaction step for the OER and the oxidation of alcohols.[36,53,55–57] Thus, both reactions will compete for this intermediate. The oxidation potential of alcohols is much lower than the one of water,[58] and, in general, alcohol oxidation has been reported to proceed quickly after *[O_e] formation.[36,59] However, for nickel based water oxidation, the consecutive reactions have been described to be the rds.[36,57,60] So, a good alcohol oxidation catalyst should easily form *[O_e] and then have higher reaction barriers for the consecutive OER steps.[53] This leads to a high selectivity toward alcohol oxidation. However, if the OER rds of a catalyst is the *[O_e] formation and the consecutive OER steps proceed quickly, it will immediately perform OER after *[O_e] formation.[36] *[O_e] formation was observed to occur simultaneously with the nickel oxidation peak at 1.36 V_{RHE} (Figure 5a,b, and Figures S20 and S21, Supporting Information),[36,38,56] which involves around 1.6 electrons per Ni^{II}.[23–26] Herein, without organic substrate, no catalytic current is observed after the nickel oxidation peak until ≈1.50 V_{RHE} (Figure 5a), most likely because a consecutive OER step requires 1.50 eV. In this potential range (1.36–1.50 V_{RHE}), the pure nickel catalyst can perform the oxidation of an alcohol without the interference of the OER which has also been shown previously by rotating ring-disk electrode measurements.[36] The incorporation of iron into the electrode has three effects (Figure 5a,b): i) it decreases the current density of selective MeOH oxidation (the current density at 1.43 V_{RHE} is around two times higher for NF-Plasma than NF-Plasma-Fe); ii) it increases the redox peak potential; and iii) it reduces the OER onset potential. Thus, the *[O_e] formation becomes more difficult while the following rds OER step becomes easier resulting in a higher OER activity that onsets directly after the redox peak.[53] Therefore, a smaller range and lower maximum potential exist where selective MeOH oxidation could be performed on NF-Plasma-Fe compared to NF-Plasma. Taken together, for a pure nickel catalyst, the rds occurs after the initial adsorption and oxidation of OH^-/H_2O (*[O_e] formation), while the initial *[O_e] formation is rate-determining for an iron-nickel catalyst. This conclusion also agrees with recent theoretical investigations.[36,57] Therefore, NF-Plasma is the less active OER but better alcohol/aldehyde oxidation catalyst. As the NF-Plasma and NF-Plasma-Fe have the same morphology and surface area (Figure 2d–h, and Figures S12b and S13, Supporting Information), the observed differences originate only from electronic and mechanistic effects.

After comparing iron-containing and iron-free samples, we arrive at the effects of the plasma treatment. NF-Plasma shows 40-times higher OER activity than NF; however, for the BA/HMF oxidation, under steady-state conditions, NF-Plasma is only around six times more active. Thus, in contrast to the OER activity, the BA/HMF oxidation activity is not proportional to e^-_{redox}. However, herein and by others, it has been proposed that both reactions have similar kinds of active sites.[36] Therefore, another effect must be responsible for the reduced activity enhancement. In this regard, the HMF/BA oxidation steady-state measurements clearly show an effect of substrate concentration and stirring revealing that the reaction is limited by substrate diffusion. During the OER, where hydroxide must be transported, no such effects have been observed, which is reasonable considering a hydroxide diffusion coefficient of 45 $\mu cm^2\ s^{-1}$ and a concentration of 1 M compared to 9.2 and 8.5 $\mu cm^2\ s^{-1}$ for HMF and BA, respectively, and a concentration of 0.1 M.[61–63] Furthermore, diffusion limitations are probably particularly relevant in this study due to the high current densities resulting from the large density of active sites or adsorbed *[O_e] per geometrical surface area electrode. Diffusion limitations in the near electrode area affect how the surface area influences the catalytic turnover. In this regard, the HMF/BA activity scales well with the six times enhanced C_{dl} while the OER activity scales with the 40-times enhanced e^-_{redox} (Figure S11, Supporting Information). **Figure 8** shows how nanostructuring of surfaces affects the electrical double-layer (EDL) and the inner Helmholtz layer (IHL) area.[64] The EDL of the anode contains more solvated anions than cations while the distribution of the two species is even in the bulk electrolyte. During the C_{dl} measurement mainly hydroxide is migrating into the EDL which is several nanometers thick.[65] The IHL is comprised of specifically adsorbed species (e.g., hydroxide or OER reaction intermediates) and thus is thinner than 0.3 nm. For the same material, e^-_{redox} should scale with the IHL area, as specific ad-/desorption of ions is required for the redox activity (e.g., $Ni(OH)_2 \rightarrow NiOOH + e^- + H^+$). The IHL area increases severely more than the EDL area, which is caused by the different thicknesses of these two layers. The larger thickness of the EDL results in a reduced sensitivity to nanostructures smaller than the EDL thickness (Figure 8b).

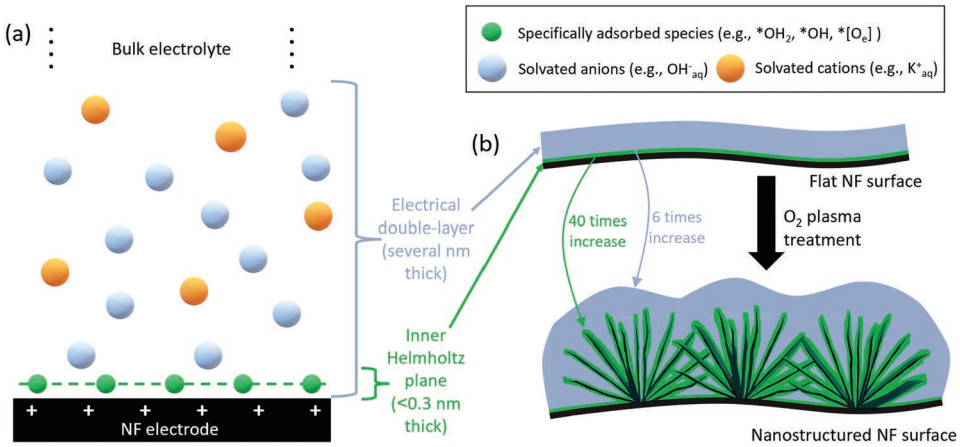

Figure 8. Scheme on the effect of surface nanostructuring of an anode on the inner Helmholtz plane (IHP) and the electrical double-layer (EDL). a) A scheme showing the IHP, which is comprised of specifically adsorbed species, and the EDL, which starts at the electrode surface until the bulk electrolyte. The EDL of an anode contains more anions than cations while both are evenly distributed in the bulk electrolyte. b) Depiction of a flat and a through plasma electrolysis obtain nanostructured NF surface with three nano-flowers. The IHP area is proportional to the green area and the EDL to the grey area. Due to the much larger thickness of the EDL compared to the IHP, the IHP area increases by several times more than the EDL area through the nanostructuring. The thickness of the diffusion layer during electrocatalytic HMF/BA oxidation with stirring seems to be comparable to the one of the EDL for hydroxide migration during the double-layer capacitance measurements.

Therefore, the green IHL area in Figure 8b shows a much stronger increase from the nanostructuring than the grey EDL area. Coming back to the HMF/BA oxidation, in a stirred electrocatalytic reaction, the simplest model for diffusion is that on the surface of the electrode a diffusion layer exists followed by a bulk solution with constant concentration.[66] A larger surface results in a larger diffusion-layer to bulk-solution interface and thus faster mass transport. In our case, the EDL thickness during mainly hydroxide migration of the C_{dl} measurements scales well with the increased diffusion during electrocatalysis, probably because the diffusion layers of both processes have comparable thicknesses. The observation that the OER scales with e^-_{redox} (scales with the IHP area) and the diffusion-controlled reaction with the C_{dl} (scales with the EDL area) also implies that the optimal electrode morphology for both processes is different.

4. Conclusion

Using a novel, glow discharge, thermal, in-liquid plasma electrolysis approach, the flat nickel foam surface was modified to a hierarchically nanostructured surface with a flower-like appearance and an increased surface area and number of active sites. This plasma electrolysis approach involves no expensive or toxic chemicals (only water and KOH), consumes little energy, takes only 10 min, and requires only a simple two-electrode setup with a high-power supply and no external heating. We could dope iron into the plasma modified NF (NF-Plasma-Fe) under retention of its surface morphology and surface area by plain cycling. In this fashion, the high surface area electrode can be chemically modified to suit various catalytic processes. The obtained electrodes are self-supported, binder free, and stable under strongly anodic catalytic conditions and heavy gas formation due to the much harsher conditions during their synthesis. When applying NF-Plasma-Fe as electrodes for the OER, an industrially relevant current density of 500 mA cm^{-2} could be achieved at 1.473 ± 0.013 V_{RHE} (60 °C) and no activity decrease could be observed over 140 h at 200 mA cm^{-2}. Furthermore, using a NF-Plasma electrode, the electrocatalytic oxidation of 5-(hydroxymethyl)furfural and benzyl alcohol with merely water as an oxygen source could be accomplished selectively at current densities up to 800 mA cm^{-2}. Moreover, we found that the OER activity scales with the amount of redox active sites and that the organic oxidation reactions are limited by diffusion. This behavior is explained with a model considering the diffusion coefficients, inner Helmholtz plain, the electrical double-layer, and the electrode morphology. In addition, we reveal that even though iron-containing samples are more active for the OER, they are less suitable for the oxidation of alcohols and aldehydes.

Supporting Information

Supporting Information is available from the Wiley Online Library or from the author.

Acknowledgements

Funded by the Deutsche Forschungsgemeinschaft (Germany's Excellence Strategy – EXC 2008/1-390540038 – UniSysCat and the German Federal Ministry of Education and Research (BMBF project "PrometH2eus", 03HY105C). P.W.M. acknowledges support from the German Federal Ministry of Education and Research in the framework of the project Catlab (03EW0015A/B). J.N.H. and K.L are indebted to the Einstein Foundation Berlin/EC2/BIG-NSE for a Ph.D. fellowship. This work was also supported by the Deutsche Forschungsgemeinschaft (DFG) through Grant No. SFB-CRC1316 (collaborative research center).

Open access funding enabled and organized by Projekt DEAL.

Conflict of Interest

The authors declare no conflict of interest.

Author Contributions

J.N.H. and P.V.M. contributed equally to this work. P.W.M. initiated the idea and developed it together with J.N.H.; J.N.H. performed the electrocatalysis experiments, analyzed all data, and wrote the first draft; P.V.M. performed the plasma synthesis and the SEM experiments; M.D., T.J., and P.W.M. supervised the study; G.V. performed the organic oxidation experiments; K.L. and I.Z. performed the Raman experiments; T.D. performed the XPS measurements. All authors discussed the results and commented on the manuscript.

Data Availability Statement

The data that support the findings of this study are available from the corresponding author upon reasonable request.

Keywords

5-(hydroxymethyl)furfural oxidation, benzyl alcohol oxidation, gamma-NiFeOOH, in-liquid oxygen plasma, nickel foam, nickel-iron oxyhydroxides, oxygen evolution reaction

Received: June 21, 2022
Revised: July 21, 2022
Published online: August 21, 2022

[1] O. J. Guerra, J. Zhang, J. Eichman, P. Denholm, J. Kurtz, B.-M. Hodge, *Energy Environ. Sci.* **2020**, *13*, 1909.
[2] Z. W. Seh, J. Kibsgaard, C. F. Dickens, I. Chorkendorff, J. K. Nørskov, T. F. Jaramillo, *Science* **2017**, *355*, eaad4998.
[3] Y. Li, X. Wei, L. Chen, J. Shi, *Angew. Chem., Int. Ed.* **2021**, *60*, 19550.
[4] L. Du, Y. Sun, B. You, *Mater. Rep. Energy* **2021**, *1*, 100004.
[5] M. Chatti, J. L. Gardiner, M. Fournier, B. Johannessen, T. Williams, T. R. Gengenbach, N. Pai, C. Nguyen, D. R. MacFarlane, R. K. Hocking, A. N. Simonov, *Nat. Catal.* **2019**, *2*, 457.
[6] Y. Lum, J. E. Huang, Z. Wang, M. Luo, D. H. Nam, W. R. Leow, B. Chen, J. Wicks, Y. C. Li, Y. Wang, C. T. Dinh, J. Li, T. T. Zhuang, F. Li, T. K. Sham, D. Sinton, E. H. Sargent, *Nat. Catal.* **2020**, *3*, 14.
[7] O. Schmidt, A. Gambhir, I. Staffell, A. Hawkes, J. Nelson, S. Few, *Int. J. Hydrogen Energy* **2017**, *42*, 30470.
[8] H. Yang, M. Driess, P. W. Menezes, *Adv. Energy Mater.* **2021**, *11*, 2102074.
[9] A. Peugeot, C. E. Creissen, D. Karapinar, H. N. Tran, M. Schreiber, M. Fontecave, *Joule* **2021**, *5*, 1281.
[10] F. Yang, K. Cheng, X. Xue, J. Yin, G. Wang, D. Cao, *Electrochim. Acta* **2013**, *107*, 194.
[11] H. Yin, L. Jiang, P. Liu, M. Al-Mamun, Y. Wang, Y. L. Zhong, H. Yang, D. Wang, Z. Tang, H. Zhao, *Nano Res.* **2018**, *11*, 3959.
[12] N. K. Chaudhari, H. Jin, B. Kim, K. Lee, *Nanoscale* **2017**, *9*, 12231.
[13] H. Zhou, F. Yu, Q. Zhu, J. Sun, F. Qin, L. Yu, J. Bao, Y. Yu, S. Chen, Z. Ren, *Energy Environ. Sci.* **2018**, *11*, 2858.
[14] X. Xu, F. Song, X. Hu, *Nat. Commun.* **2016**, *7*, 12324.
[15] S. Sikdar, P. V. Menezes, R. Maccione, T. Jacob, P. L. Menezes, *Nanomaterials* **2021**, *11*, 1375.
[16] S. Dou, L. Tao, R. Wang, S. El Hankari, R. Chen, S. Wang, *Adv. Mater.* **2018**, *30*, 1705850.
[17] H. Liang, F. Ming, H. N. Alshareef, *Adv. Energy Mater.* **2018**, *8*, 1801804.
[18] D. Wang, Y. Zou, L. Tao, Y. Zhang, Z. Liu, S. Du, S. Zang, S. Wang, *Chin. Chem. Lett.* **2019**, *30*, 826.
[19] M. D. Klapkiv, *Mater. Sci.* **1996**, *31*, 494.
[20] D. Y. Chung, P. P. Lopes, P. F. B. D. Martins, H. He, T. Kawaguchi, P. Zapol, H. You, D. Tripkovic, D. Strmcnik, Y. Zhu, S. Seifert, S. Lee, V. R. Stamenkovic, N. M. Markovic, *Nat. Energy* **2020**, *5*, 222.
[21] J. N. Hausmann, S. Mebs, K. Laun, I. Zebger, H. Dau, P. W. Menezes, M. Driess, *Energy Environ. Sci.* **2020**, *13*, 3607.
[22] J. N. Hausmann, B. Traynor, R. J. Myers, M. Driess, P. W. Menezes, *ACS Energy Lett.* **2021**, *6*, 3567.
[23] D. A. Kuznetsov, B. Han, Y. Yu, R. R. Rao, J. Hwang, Y. Román-Leshkov, Y. Shao-Horn, *Joule* **2018**, *2*, 225.
[24] M. Merrill, M. Worsley, A. Wittstock, J. Biener, M. Stadermann, *J. Electroanal. Chem.* **2014**, *717–718*, 177.
[25] D. A. Corrigan, R. M. Bendert, *J. Electrochem. Soc.* **1989**, *136*, 723.
[26] It has been proposed that this Ni^{II} oxidation involves 1-1.6 electrons per Ni site.[23–25] Herein, we merely use this parameter to compare the plasma and not plasma-treated samples relatively toward each other. We assume that the numbers of electrons transferred per nickel site are the same in the non-plasma-treated and the plasma-treated samples. Therefore, for this relative comparison, it is not necessary to assume how many electrons are transferred per Ni site. However, for the calculation of the turnover frequencies of Figure 4g, we assumed that 1.6 electrons per nickel site were transferred. More information on the turnover frequency calculations can be found in the Supporting Information.
[27] M. B. Stevens, C. D. M. Trang, L. J. Enman, J. Deng, S. W. Boettcher, *J. Am. Chem. Soc.* **2017**, *139*, 11361.
[28] A. P. Grosvenor, M. C. Biesinger, R. S. C. Smart, N. S. McIntyre, *Surf. Sci.* **2006**, *600*, 1771.
[29] M. C. Biesinger, B. P. Payne, A. P. Grosvenor, L. W. M. Lau, A. R. Gerson, R. S. C. Smart, *Appl. Surf. Sci.* **2011**, *257*, 2717.
[30] H. W. Nesbitt, D. Legrand, G. M. Bancroft, *Phys. Chem. Miner.* **2000**, *27*, 357.
[31] G. C. Allen, M. T. Curtis, A. J. Hooper, P. M. Tucker, *J. Chem. Soc., Dalton Trans.* **1974**, 1525.
[32] J. N. Hausmann, R. Beltrán-Suito, S. Mebs, V. Hlukhyy, T. F. Fässler, H. Dau, M. Driess, P. W. Menezes, *Adv. Mater.* **2021**, *33*, 2008823.
[33] M. S. Burke, S. Zou, L. J. Enman, J. E. Kellon, C. A. Gabor, E. Pledger, S. W. Boettcher, *J. Phys. Chem. Lett.* **2015**, *6*, 3737.
[34] S. Lee, L. Bai, X. Hu, *Angew. Chem., Int. Ed.* **2020**, *59*, 8072.
[35] M. B. Stevens, L. J. Enman, A. S. Batchellor, M. R. Cosby, A. E. Vise, C. D. M. Trang, S. W. Boettcher, *Chem. Mater.* **2017**, *29*, 120.
[36] H. B. Tao, Y. Xu, X. Huang, J. Chen, L. Pei, J. Zhang, J. G. Chen, B. Liu, *Joule* **2019**, *3*, 1498.
[37] A. M. Ullman, C. N. Brodsky, N. Li, S. L. Zheng, D. G. Nocera, *J. Am. Chem. Soc.* **2016**, *138*, 4229.
[38] O. Diaz-Morales, D. Ferrus-Suspedra, M. T. M. Koper, *Chem. Sci.* **2016**, *7*, 2639.
[39] S. Lee, K. Banjac, M. Lingenfelder, X. Hu, *Angew. Chem., Int. Ed.* **2019**, *58*, 10295.
[40] C. Hu, Y. Hu, C. Fan, L. Yang, Y. Zhang, H. Li, W. Xie, *Angew. Chem., Int. Ed.* **2021**, *60*, 19774.
[41] J. R. Swierk, S. Klaus, L. Trotochaud, A. T. Bell, T. D. Tilley, *J. Phys. Chem. C* **2015**, *119*, 19022.
[42] G. George, S. Anandhan, *RSC Adv.* **2014**, *4*, 62009.
[43] D. Chen, X. Xiong, B. Zhao, M. A. Mahmoud, M. A. El-Sayed, M. Liu, *Adv. Sci.* **2016**, *3*, 1500433.
[44] M. Fleischmann, K. Korinek, D. Pletcher, *J. Chem. Soc., Perkin Trans.* **1972**, *2*, 1396.
[45] M. T. Bender, Y. C. Lam, S. Hammes-Schiffer, K.-S. Choi, *J. Am. Chem. Soc.* **2020**, *142*, 21538.
[46] J. A. Matthews, *Encyclopedia of Environmental Change*, Sage Publications Ltd., London, UK **2014**.
[47] T. Pfennig, J. M. Carraher, A. Chemburkar, R. L. Johnson, A. T. Anderson, J.-P. Tessonnier, M. Neurock, B. H. Shanks, *Green Chem.* **2017**, *19*, 4879.
[48] N. Brun, P. Hesemann, D. Esposito, *Chem. Sci.* **2017**, *8*, 4724.

[49] H. Huang, C. Yu, X. Han, H. Huang, Q. Wei, W. Guo, Z. Wang, J. Qiu, *Energy Environ. Sci.* **2020**, *13*, 4990.
[50] D. H. Nam, B. J. Taitt, K. S. Choi, *ACS Catal.* **2018**, *8*, 1197.
[51] W.-J. Liu, L. Dang, Z. Xu, H.-Q. Yu, S. Jin, G. W. Huber, *ACS Catal.* **2018**, *8*, 5533.
[52] S. Anantharaj, S. Kundu, S. Noda, *Nano Energy* **2021**, *80*, 105514.
[53] N. Heidary, N. Kornienko, *Chem. Sci.* **2020**, *11*, 1798.
[54] R. Gottschall, R. Schöllhorn, M. Muhler, N. Jansen, D. Walcher, P. Gütlich, *Inorg. Chem.* **1998**, *37*, 1513.
[55] H. Zhou, Z. Li, S. Xu, L. Lu, M. Xu, K. Ji, R. Ge, Y. Yan, L. Ma, X. Kong, L. Zheng, H. Duan, *Angew. Chem., Int. Ed.* **2021**, *60*, 8976.
[56] D. Drevon, M. Görlin, P. Chernev, L. Xi, H. Dau, K. M. Lange, *Sci. Rep.* **2019**, *9*, 1532.
[57] H. Xiao, H. Shin, W. A. Goddard III, *Proc. Natl. Acad. Sci. USA* **2018**, *115*, 5872.
[58] M. I. Abdullah, A. Hameed, N. Zhang, M. H. Islam, M. Ma, B. G. Pollet, *ACS Appl. Mater. Interfaces* **2021**, *13*, 30603.
[59] B. Mondal, N. Karjule, C. Singh, R. Shimoni, M. Volokh, I. Hod, M. Shalom, *Adv. Energy Mater.* **2021**, *11*, 2101858.
[60] A. G. Rajan, J. M. P. Martirez, E. A. Carter, *J. Am. Chem. Soc.* **2020**, *142*, 3600.
[61] S. H. Lee, J. C. Rasaiah, *J. Chem. Phys.* **2011**, *135*, 124505.
[62] F. Gharagheizi, *Ind. Eng. Chem. Res.* **2012**, *51*, 2797.
[63] K. Yui, N. Yamazaki, T. Funazukuri, *J. Chem. Eng. Data* **2013**, *58*, 183.
[64] M. Dunwell, Y. Yan, B. Xu, *Curr. Opin. Chem. Eng.* **2018**, *20*, 151.
[65] G. Li, L. Anderson, Y. Chen, M. Pan, P. Y. A. Chuang, *Sustainable Energy Fuels* **2018**, *2*, 237.
[66] A. J. Bard, L. R. Faulknes, *Electrochemical Methods: Fundamentals and Applications*, John Wiley & Sons, Ind, New York **2001**.